Article:
Hume, E., Köster, P., Baffigi, F. et al. (12 more authors) (2025) An investigation of the emittance of escaping fast electron beams from planar and nanowire targets. High Power Laser Science and Engineering. e14. ISSN 2052-3289

https://doi.org/10.1017/hpl.2025.5

High Power Laser Science and Engineering, (2025), Vol. 13, e14, 10 pages.
doi:10.1017/hpl.2025.5

RESEARCH ARTICLE

An investigation of the emittance of escaping fast electron beams from planar and nanowire targets

E. J. Hume[1], P. Köster[1], F. Baffigi[1], F. Brandi[1], D. Calestani[2], G. Cristoforetti[1], L. Fulgentini[1], L. Labate[1], A. Marasciulli[1,5], S. Morris[3], D. Palla[1], M. Salvadori[1], M. Villani[2], L. A. Gizzi[1], and K. L. Lancaster[4]

[1]*Intense Laser Irradiation Laboratory (ILIL), INO-CNR, Pisa, Italy*

[2]*IMEM-CNR, Parma, Italy*

[3]*Department of Physics, University of Warwick, Coventry, UK*

[4]*York Plasma Institute, University of York, York, UK*

[5]*Current address: INFN Laboratori Nazionali del Gran Sasso, LNGS-INFN, Assergi, AQ, Italy*

(Received 17 September 2024; revised 20 November 2024; accepted 31 December 2024)

Abstract

Fast electron generation and transport in high-intensity laser–solid interactions induces X-ray emission and drives ion acceleration. Effective production of these sources hinges on an efficient laser absorption into the fast electron population and control of divergence as the beam propagates through the target. Nanowire targets can be employed to increase the laser absorption, but it is not yet clear how the fast electron beam properties are modified. Here we present novel measurements of the emittance of the exiting fast electron beam from irradiated solid planar and nanowire targets via a pepper-pot diagnostic. The measurements indicate a greater fast electron emittance is obtained from nanowire targets. Two-dimensional particle-in-cell simulations support this conclusion, revealing beam defocusing at the wire–substrate boundary, a higher fast electron temperature and transverse oscillatory motion around the wires.

Keywords: emittance; fast electrons; femtosecond; particle-in-cell; pepper-pot

1. Introduction

Beams of MeV-energy fast electrons can be created via irradiation of high-intensity $\left(I\lambda^2 > 10^{18}\ \mathrm{W\,cm^{-2}\,\mu m^2}\right)$, femtosecond laser pulses with solid targets. These fast electrons propagate through the target and are the driver of much of the downstream physics during the interaction. As the fast electron beam propagates through the target it induces bremsstrahlung emission that can be used as a high-energy X-ray source for radiography[1]. The fast electrons additionally cause fluorescence of kα X-rays in the material, enabling the characterization of warm dense matter produced in the interaction[2,3]. The highest energy electrons can escape the target at the rear surface[4], driving an electrostatic sheath field that can additionally accelerate protons up to MeV energies[5–7]. These ion beams could find use in medical applications[8] and as a source of protons for diagnosing warm, dense matter[9]. Moreover, the fast electron beam itself has been proposed as an igniter in the fast ignition (FI) variant of inertial confinement fusion[10].

Characterization of the fast electrons is crucial to determine suitable applications of these sources. The energies of the escaping fast electron beam can be measured to recover the energy spectra of the fast electron population[11]. In a study by Honrubia and Meyer-ter-Vehn[12], the energy fraction deposited into FI-relevant dense targets was found to be sensitive to the average kinetic energy of the beam, demonstrating that the efficiency of the interaction has a dependence on the electron energy spectra. It is well-established that the fast electron beam possesses an intrinsic divergence[13,14]; in the context of FI this could result in energy deposition occurring over a larger volume than the hotspot volume[15]. The divergence of the beam can also influence the properties of bremsstrahlung X-ray emission, as highlighted by Armstrong *et al.*[16], where it was found that a reduction of the divergence yielded a preferential source for imaging. In addition, the divergence of the beam results in a reduced current density j_f at the rear target

Correspondence to: E. J. Hume, Intense Laser Irradiation Laboratory (ILIL), INO-CNR, Pisa 56124, Italy. Email: emmajane.hume@ino.cnr.it

surface. This can be of detriment to the maximum energies of ions accelerated under the target normal sheath acceleration (TNSA) mechanism, demonstrated via a theoretical model by Mora[17] and Bayesian analysis by Takagi *et al.*[18].

In general, an electron beam is characterized by the emittance, a measure of the area of position-momentum space occupied by the electron population[19–21]. The total root mean square (rms) emittance of a population of particles along the transversal x-axis can be given as follows:

$$\epsilon_x = \sqrt{< x^2 >< x'^2 > - < xx' >^2}, \tag{1}$$

where x is the particle position and x' is the particle momentum. The emittance encompasses information on the divergence of the electrons, the electron Lorentz factor related to its momentum and the source size. Thus, the emittance can be a useful figure-of-merit to characterize a beam since it is a conserved quantity of the beam (for conservative forces). For applications one can imagine a beam with a smaller emittance might be preferable since this implies that a focused, monoenergetic beam has been obtained. From the perspective of understanding laser–plasma interactions, the measurement of the emittance can indeed be a valuable tool for uncovering information about the electron momentum distribution, which can provide information on the absorption mechanism(s) at play.

Many fast electron transport studies have employed planar foil targets. More recently, the use of nanowire (NW) targets has attracted growing interest on account of an observed increase in laser absorption[22–26]. Due to the relative novelty of these targets open questions remain on the influence of the wires on the absorption, fast electron generation and transport and the beam properties. An increased temperature of the fast electron population has been frequently reported from these NW targets[27–30], which could correlate with an increase in the phase space and thus the emittance of the electrons. Jiang *et al.*[31] proposed a target design with 'tower' structures on the front surface that facilitated the generation of higher energy electrons concurrent with a narrower angular cone of emission when compared to planar targets. The simulations used a large wire spacing with respect to the laser spot size (2 μm vacuum gap size and 2.9 μm full width at half maximum (FWHM) spot size), which facilitated the direct laser acceleration (DLA) mechanism, and only considered the highest energy electrons that were considered to be optimally positioned to undergo DLA. Imaging of X-ray emission at the front and rear surfaces of nanobrush targets by Zhao *et al.*[32] suggested collimation of the electron beam by the wire-like front structures. However, there is little other recorded experimental evidence of this guiding effect. Furthermore, it is not clear how, or indeed if, this guiding translates into an effect on the emittance of the exiting fast electron beam.

In this paper we present the first experimental measurements of the emittance of the exiting fast electron beam generated from intense laser interactions with solid targets. A pepper-pot diagnostic was employed to obtain transverse emittance estimates in a novel measurement for fast electrons generated from laser–solid interactions. The results indicate an increased emittance of the electron beam generated from the NW target compared to the planar target. Simulations using the two-dimensional (2D) particle-in-cell (PIC) code EPOCH are used to elucidate the fast electron transport along the wires. We show that electrons with energies close to the ponderomotive energy are confined to the wires by the electromagnetic (EM) fields established around the structures. In addition, the simulations reveal the growth of a defocusing magnetic field at the wire–substrate boundary that can strongly influence the fast electron transport and the overall beam emittance.

2. Pepper-pot diagnostic

A pepper-pot diagnostic can be used to obtain an estimate of the electron beam emittance[19,33]. The setup of a pepper-pot diagnostic is depicted in Figure 1. The approach involves passing the beam of particles through a mask with an array of holes of known diameter and spacing. This divides the larger beam into several smaller beamlets. These beamlets propagate a distance, L, from the pepper-pot mask to a detector. Since the particle population will possess some transverse momenta, there will be a net shift of the beamlet position with respect to the original position at the pepper-pot mask. An estimate of the transverse emittance is then possible from coupling information on the dimensions and relative positions of the holes in the mask, and the beamlets at the detector. A derivation carried out by Zhang[34] demonstrated that Equation (1) can be rewritten for the case of a subset of N particles from a larger population of particles as follows:

$$\epsilon_x^2 \approx \frac{1}{N^2}\left\{\sum_{j=1}^{p} n_j\left(x_{hj}-\bar{x}\right)^2 \cdot \sum_{j=1}^{p}\left[n_j\sigma_{x'_j}^2 + n_j\left(\bar{x}'_j-\bar{x}'\right)^2\right] - \left(\sum_{j=1}^{p} n_j x_{hj}\bar{x}'_j - N\bar{x}\bar{x}'\right)^2\right\}, \tag{2}$$

where p is the number of holes, x_{hj} is the position of the hole, n_j is the number of electrons within the beamlet, N is the total number of electrons, $\sum_{j=1}^{p} n_j$, $\bar{x}$ is the mean position of all beamlets, $\bar{x}'_j$ is the mean divergence of the jth beamlet, $\bar{x}'$ is the mean divergence of all beamlets and $\sigma_{x'_j}$ is the mean rms spot size of the jth beamlet at the jth hole.

The mean divergence can be retrieved from the hole and beamlet positions as $\bar{x}'_j = \left(\bar{X}_j - x_{hj}\right)/L$, where L is the distance between the pepper-pot mask and film, and we

https://doi.org/10.1017/hpl.2025.5 Published online by Cambridge University Press

assume the small angle approximation is valid. The pepper-pot samples only the fraction of the fast electron beam that propagates through the holes in the mask. Thus, the value obtained from this method can only be taken as an approximation of the population.

3. Experimental results

The experimental work was conducted at the ILIL facility at INO-CNR, Pisa[35]. The ILIL-PW Ti:sapphire laser line was used to irradiate both planar and NW-coated targets. The NWs were produced via chemical bath deposition[36] onto a 5 μm planar Ti substrate, and comprised 6 μm long ZnO wires of average diameter 390 ± 50 nm with an average vacuum gap of 400 ± 200 nm between the wires. The planar targets were 12.5 μm thick Ti foil, comparable to the total thickness of the NW targets (11 μm).

An acknowledged concern with the use of nanostructured targets in intense laser interactions is the disruption of the structures by the laser pedestal or pre-pulses prior to the arrival of the main pulse[37]. The use of a high-contrast laser profile can improve the prospects of retaining the structures until the main pulse interaction. One approach is to frequency double the laser pulse with an appropriate non-linear crystal. In the experiment, second harmonic generation of the 800 nm laser pulse was achieved using a potassium dihydrogen phosphate (KDP) crystal placed immediately after the compressor, creating pulses with a wavelength $\lambda_{2\omega} \sim 400$ nm. The length of the 800 nm pulse post-compression is 27 fs, which after propagation through the KDP crystal yields a 400 nm pulse with approximate duration of 80 fs FWHM. The laser pulse is reflected off two blue mirrors to remove unconverted 800 nm light and one metallic mirror before striking a silver-coated $f/\sim 4.5$ off-axis parabolic (OAP) mirror, focusing the laser to an

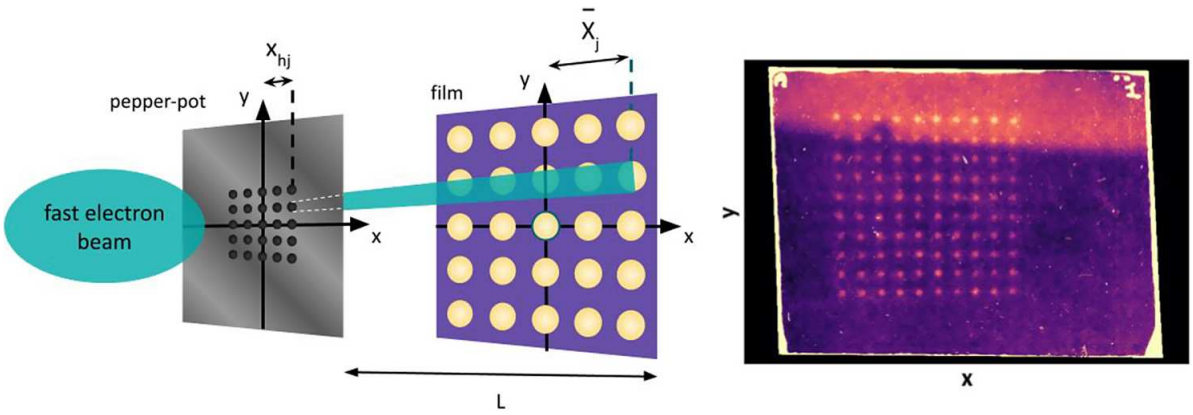

Figure 1. Illustration of the pepper-pot setup. In this configuration the fast electrons propagate from left to right. The image on the far-right shows a sample of the raw data obtained from the experimental work in this paper.

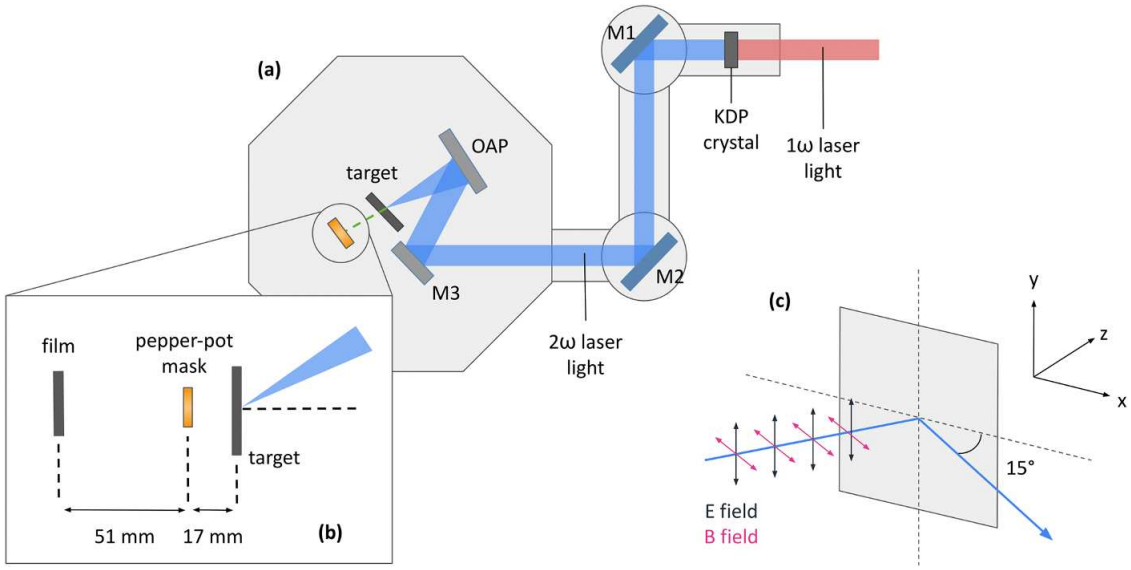

Figure 2. (a) Layout of the experimental setup in the vacuum chamber. A pepper-pot diagnostic is placed behind the irradiated target; (b) shows the setup of the pepper-pot. (c) The orientation of the laser fields with respect to the target.

https://doi.org/10.1017/hpl.2025.5 Published online by Cambridge University Press

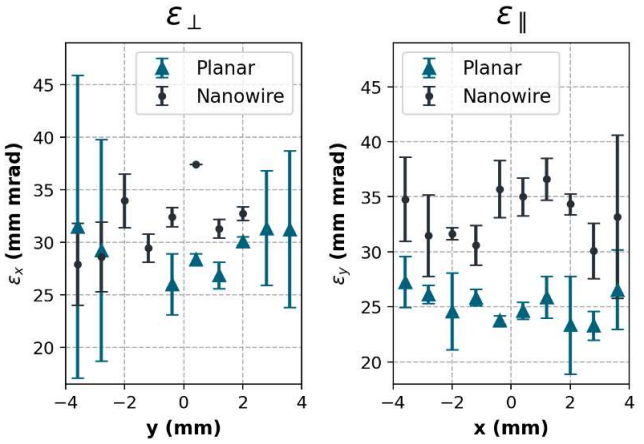

Figure 3. Experimental estimate of the transverse emittance in (a) x, perpendicular to the laser **E**-field, and (b) y, parallel to the **E**-field. Error bars are taken from the uncertainty introduced from the background correction applied.

elliptical focal spot of size 3.5 μm × 4.2 μm on-target. The laser irradiates the target at an incidence angle of 15°. The frequency doubling process rotates the polarization such that the 2ω pulse is s-polarized (**E**-field oscillation is in the y-direction), as indicated in Figure 2(c). Energy in the pulse at the fundamental frequency, ω_L, is 5.40 J, with 60% of the energy on-target and 60% of this energy contained within the focal spot. The $2\omega_L$ conversion efficiency is estimated to be approximately 20%, resulting in an estimated energy of 0.4 J in the focal spot. The final intensity on-target is therefore $I \approx 3.9 \times 10^{19}$ W/cm^2.

As anticipated, the emittance of the exiting fast electron beam is estimated using a pepper-pot diagnostic setup. Figure 2(a) shows the positioning of the pepper-pot in the target chamber. The pepper-pot mask has a 10 × 10 array of 0.2 mm diameter holes spaced 0.8 mm apart, and is placed at a distance of 17 mm from the rear of the target. An EBT3 film is placed at a distance of 51 mm from the pepper-pot mask to serve as the detector for the sampled fast electrons.

The emittance formula in Equation (2) is used to calculate a transverse fast electron emittance in x (perpendicular to the laser **E**-field) and y (parallel) directions from the data obtained from the irradiated planar and NW targets. Each dataset is integrated over two shots for each target type. The dominant error for these measurements is the background correction. The background signal was found to be inhomogeneous, and the upper and lower bounds on each emittance value are taken from analysis cases where the background was taken either above or below the beamlets. Figure 3(a) shows the transverse emittance $\epsilon_\perp$ calculated for each column of measured beamlets from the pepper-pot diagnostic. The fast electrons generated from the laser–NW interaction are generally found to have a larger value of $\epsilon_\perp$ than from the interaction with the planar targets, with average values of $\epsilon_\perp = 32 \pm 7$ and 29 ± 20 mm · mrad for the NW and planar targets, respectively. This result of an increased emittance for electrons accelerated from the NW targets is mirrored in the measurements of $\epsilon_\parallel$ shown in Figure 3(b). The average values are $\epsilon_\parallel = 33 \pm 10$ mm · mrad for the NW targets and $\epsilon_\parallel = 25 \pm 8$ mm · mrad for the planar targets.

4. Particle-in-cell simulations

Simulations using the PIC code EPOCH[38] are carried out to explore the laser interaction with the NW and planar targets. A domain is established of size 10 μm × 12 μm with cells of size 2.5 nm × 2.5 nm. The planar target is modelled as 8 μm thick Ti at solid density $n_i = 5.67 \times 10^{29}$ m^{-3}. The NW target is composed of Ti wires of diameter and gap size 0.4 μm and length of 6 μm. The wires are set to half-solid density, and a 2 μm thick solid density Ti planar substrate is placed behind the wires. Figures 4(a) and 4(b) show the initial electron density of the planar and NW targets at $t = 0$ fs. A reduced target thickness is employed to maintain reasonable computational costs. The focus of the investigation is on the laser–solid interaction at the planar surface and around the wires, which is satisfied without the requirement of a thicker bulk target. An average ionization $\overline{Z} = 10$ is used with the pseudoparticles at an initial temperature of 100 eV. The Ti ion species is represented by 20 pseudoparticles per cell, and the electron species represented by 200 pseudoparticles per cell. Collisions are turned on with $\ln \Lambda = 3$.

The $\lambda = 400$ nm laser enters the domain from the left-hand side and strikes the target at an incidence angle of 15°. The pulse contains 0.39 J in a Gaussian focal spot of size $d_{FWHM} = 4$ μm and a pulse length $\tau_{FWHM} = 80$ fs, corresponding to an on-target intensity $I = 3.9 \times 10^{19}$ W/cm^2 and is turned off at $t = 100$ fs.

In the PIC simulations the laser propagates in the z-direction and the transverse properties of the fast electrons are taken in the x-direction (in two dimensions we cannot explore the y-direction). Therefore, in order to explore both $\epsilon_\perp$ and $\epsilon_\parallel$ in a 2D geometry, simulations were performed for both s- and p-laser polarizations. When comparing the results from planar and NW targets the focus is on the p-polarization case. Although the experimental interaction was s-polarized, a clearer difference in emittance measurements between planar and NW targets was observed in the direction parallel to the **E**-field. This can be explored with the p-polarized 2D simulations.

4.1. Fast electron properties

A probe plane is placed at $z = 6.5$ μm to collect information on the propagating fast electrons with $E \geq 50$ keV. Whilst the simulations of the planar and NW targets are performed with a substrate thickness different from the real cases, the electron energy distribution for $E > 50$ keV will not be

https://doi.org/10.1017/hpl.2025.5 Published online by Cambridge University Press

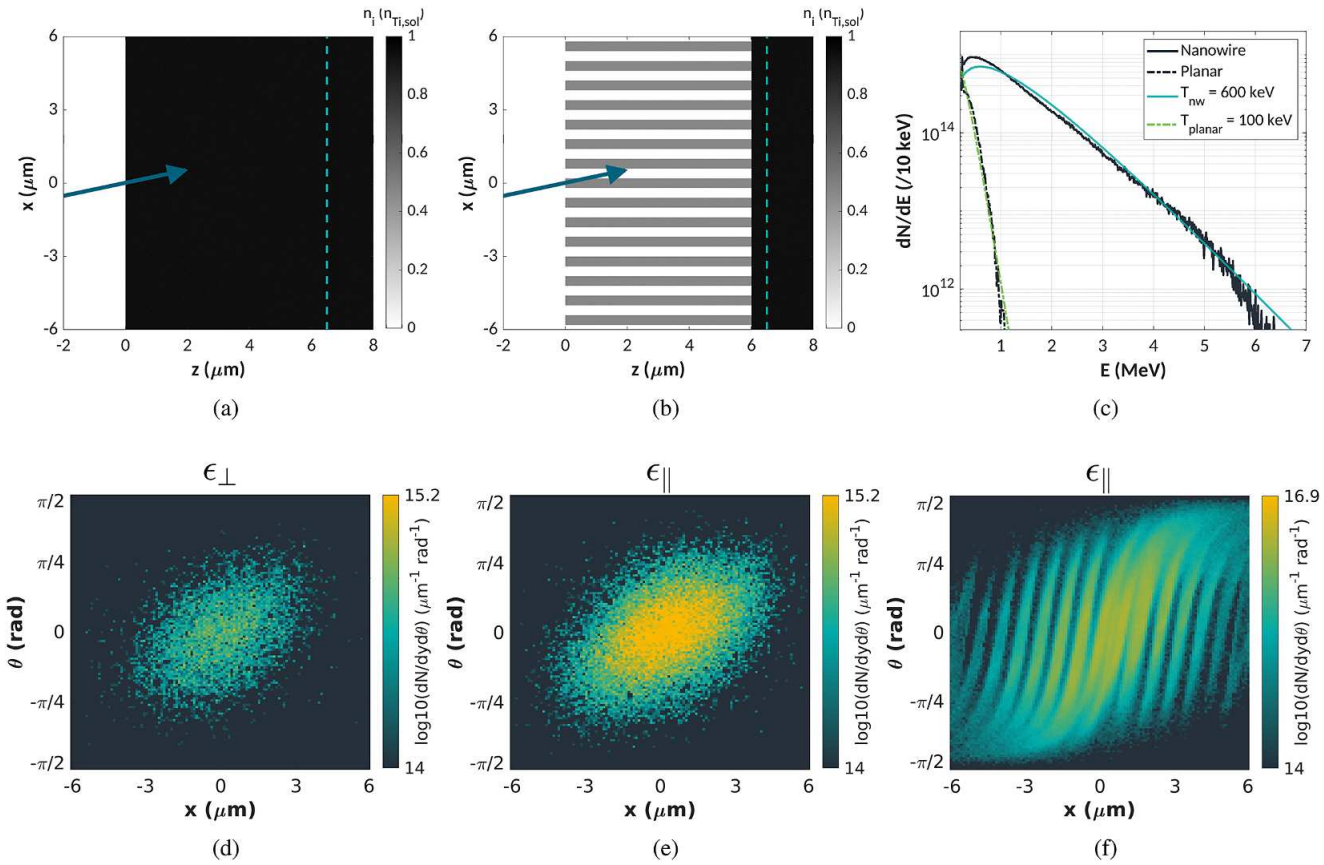

Figure 4. Initial ion density of the (a) planar and (b) nanowire targets modelled in the PIC simulations. The arrow indicates the direction of the incoming laser, irradiating the targets at an angle of 15°. The dashed line indicates the position of the probe plane. The energy spectra of the fast electrons are shown in (c) for the planar and nanowire targets. Plots (d)–(f) show the angular emittance of the fast electrons recorded at the probe plane for the different cases. In (d) the transverse emittance from the s-polarized planar case is shown, which corresponds to the emittance perpendicular to the laser **E**-field. Plots (e) and (f) show the transverse emittance obtained from the p-polarized interactions with the planar and nanowire targets, respectively. These correspond to the emittance parallel to the laser **E**-field.

significantly affected by collisions during propagation through these substrate thicknesses. Thus, the probe output can be used as an indicator of the injected fast electron energy spectra. The momentum, p, of each passing electron is used to construct an energy spectrum with bins of 10 keV for the p-polarized simulations. A best fit is found to each spectrum of the form $f(E, T_{\text{hot}}) = \frac{\gamma p}{A} \exp(-E/k_{\text{B}}T_{\text{hot}})$, where γ is the relativistic Lorentz factor, T_{hot} is the hot electron temperature and A is a normalization constant. A fit is found to the electron spectra from the planar target with a temperature $T_{\text{hot}} = 100$ keV. The hot electron temperatures predicted by the Wilks ponderomotive[39] and Sherlock[40] scalings are $T_{\text{h}} = 400$ keV and 240 keV, respectively. In comparison, the electron spectra produced from the NW targets can be described by a fit with a temperature $T_{\text{hot}} = 600$ keV, an enhancement relative to the planar target and to the classical hot electron temperature estimates.

An estimate of the emittance of the injected fast electron beams in the planar and NW targets can also be obtained from the diagnostic probe. The crossing position x and angle $\theta = \arctan(p_x/p_z)$ are recorded for each electron passing the probe plane, and are used to generate propagation angle-position plots for the fast electron beam. Figures 4(d) and 4(e) show the angle-position plots from the s-polarized and p-polarized laser–planar interactions, respectively. The p-polarized interaction yields a slightly larger emittance (ϵ_y) and higher flux of fast electrons than the s-polarized interaction (ϵ_x). In contrast, the measurements from the pepper-pot suggest the average electron emittance from the planar targets is greater along the direction of the **E**-field oscillation. However, the uncertainty introduced during analysis results in the estimates of ϵ_x and ϵ_y lying within error of each other and becoming comparable.

A similar emittance plot is constructed for the fast electrons from the NW target. Figure 4(f) shows a highly structured profile with a fraction of the electrons remaining close to the central positions of the wires with a low angular divergence, supporting the argument that the wires can sustain some guiding up to the substrate. The electrons possess a large angular spread from each wire up to $\pm\pi/2$, greater than the angular spread observed from the planar interaction. The plots here reveal a greater overall area in propagation

https://doi.org/10.1017/hpl.2025.5 Published online by Cambridge University Press

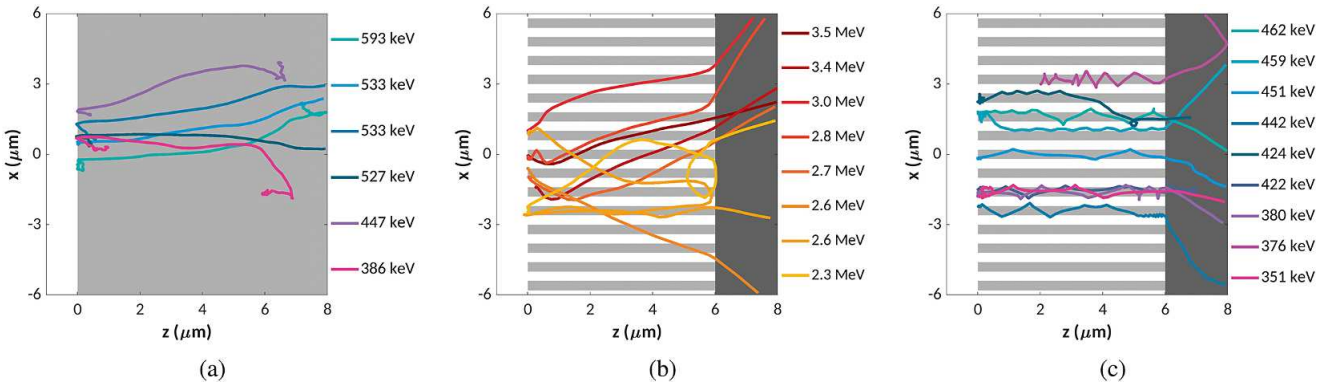

Figure 5. Electron trajectories from a random subset of hot electrons from the p-polarized laser interactions. The electron path is plotted across 120 fs, and is labelled according to the maximum energy reached during the simulation. Figures (a) and (b) show example trajectories of the highest energy electrons for the planar and nanowires respectively, and (c) shows example trajectories of lower energy electrons with $E_{\max} \sim 400$ keV from the nanowire interaction.

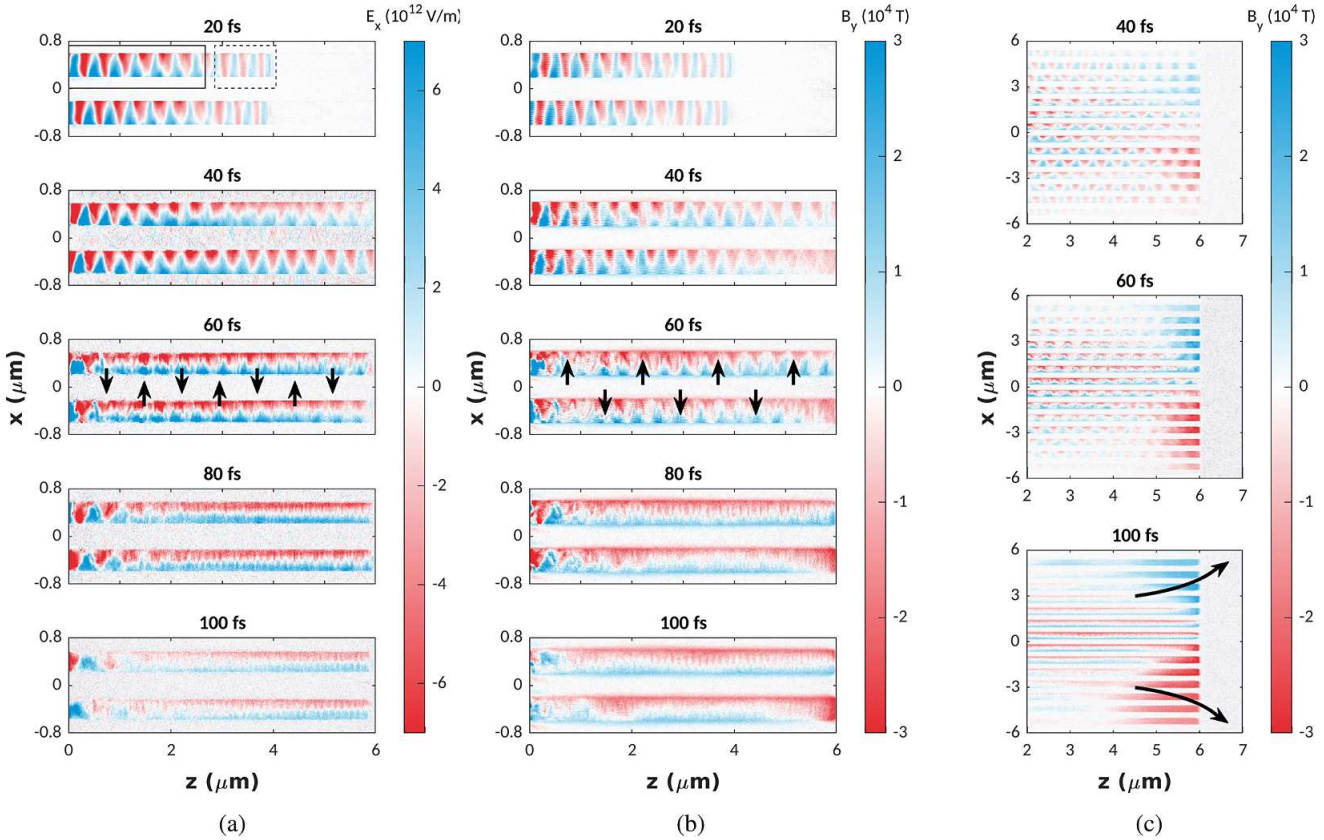

Figure 6. (a) E_x and (b) B_y field components around the central wire for the p-polarized PIC simulation. Black arrows indicate the direction on which the fields will act on an electron propagating in the z-direction. The B_y field is shown in (c) across the whole target. The black arrows here indicate the direction of deflection of an electron propagating in the $+z$-direction.

angle-position space is occupied by the fast electrons produced in the NW target, in agreement with the experimental estimate.

4.2. *Electron trajectories*

The trajectories of a random subset of individual particles can be extracted from the PIC simulations in order to delve into the influence of the wires on the electron transport. Figure 5(a) shows the trajectories of the highest energy electrons from the p-polarized interaction with the planar target. The electrons are injected at an angle along the laser **k**-vector direction, indicating we are in a regime where the electrons are primarily heated by ponderomotive acceleration for the planar targets.

The emittance plot in Figure 4(f) indicates the wires are influencing the transport of the fast electrons. Figure 5(b)

https://doi.org/10.1017/hpl.2025.5 Published online by Cambridge University Press

shows the paths travelled by electrons heated to a maximum energy $E_{max} > 2$ MeV. The electron trajectories are largely unaltered by the neighbouring wires and can propagate across the array. Upon reaching the wire–substrate boundary at $z = 6$ μm, the paths of some electrons exhibit a deflection, increasing the overall angular extent of the fast electrons as they propagate into the substrate. In contrast, the trajectories of lower energy electrons in Figure 5(c) demonstrate a clear guiding effect of the wires. The electrons are either directed along the wire surface or reflux around the wires, with the effect persisting along the whole length of the wire. Upon reaching the solid substrate this guiding effect is lost and a deflection of the electrons is again observed for some electron trajectories.

4.3. EM field growth

The EM fields around the wires are inspected to explain the trajectories of the fast electrons revealed in the simulations. Figures 6(a) and 6(b) show the evolution of the E_x and B_y components around the central wire. In Figure 6(a) at 20 fs there is propagation of the laser fields down the vacuum channels at early times, visible in the region indicated by the dashed lines. Proceeding with the initial laser propagation the field structure is reminiscent of a transverse electromagnetic (TEM) eigenmode, seen in the region selected with the solid rectangle. This can be attributed to the excitation of surface plasmon polaritons (SPPs) at the plasma–vacuum interface[41–43]. At later times a more homogeneous field structure is apparent, orientated along the wire edges.

In addition to the 'local' fields around a single wire, it can be instructive to also look at the 'global' fields across the larger simulation domain. Figure 6(c) shows the B_y component across all wires and the substrate. As early as 40 fs we are able to identify the growth of an azimuthal magnetic field at the wire–substrate boundary, which continues to grow in strength over the laser pulse time of 100 fs. Chatterjee *et al.*[44] previously reported the growth of strong self-generated magnetic fields at the rear target–vacuum boundary from fs-interactions with nanochannel targets; our simulations suggest these azimuthal fields can additionally grow to kT-levels at the wire–substrate interface.

5. Discussion

PIC simulations have revealed the evolution of strong electric and magnetic fields around the wires that affect the fast electron transport. At early times the fields inside the NW channels due to laser propagation and SPP excitation can extract and accelerate electrons from the wires[45]. At later times a prominent quasistatic field structure is instead evident. As the electrons are extracted from the wires, a charge separation will be established between the wire and vacuum regions. This will result in the generation of an electrostatic E_x field between the wires.

Figure 7(a) shows the averaged current densities along the wires at a time $t = 80$ fs. There is a net negative current density in the vacuum gaps, corresponding to electrons propagating in the $+z$-direction towards the substrate. This is neutralized within the wires due to the drawing of a return current. A net positive current is observed at the wire edges. The current density gradient between the wire and the vacuum could therefore explain the **B**-field growth observed in the simulations. Previous works have identified the drawing of the return current down the wires as the primary source of azimuthal **B**-field growth at the wires[46–48].

For an electron propagating along a wire in z, the B_y field will act to expel the electron from the wire, whereas the E_x field will draw the electron back in. This will result in a 'push–pull' net effect on an individual electron[46,49].

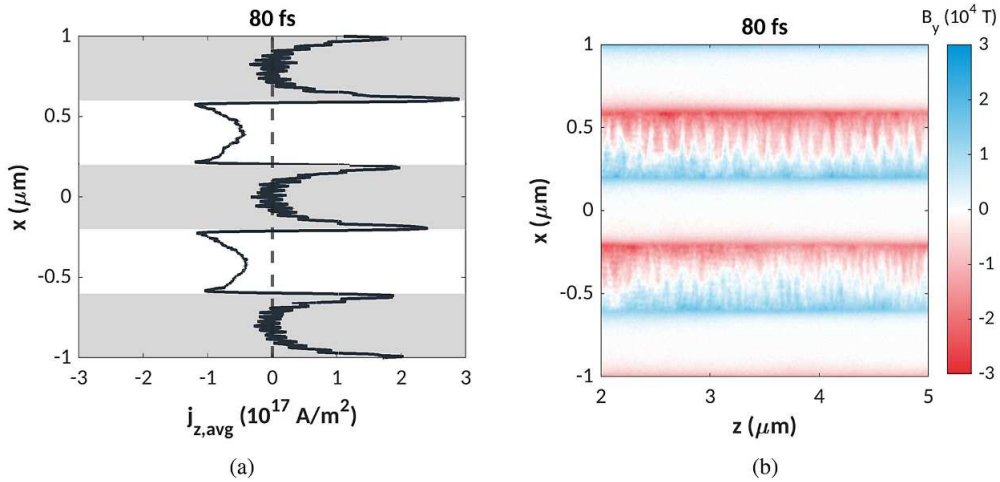

Figure 7. (a) Current density j_z averaged in the range $z = 2$–5 μm. Shaded regions indicate the wire positions and the white regions indicate vacuum. (b) Corresponding B_y fields (orthogonal to the simulation plane) within the same region.

https://doi.org/10.1017/hpl.2025.5 Published online by Cambridge University Press

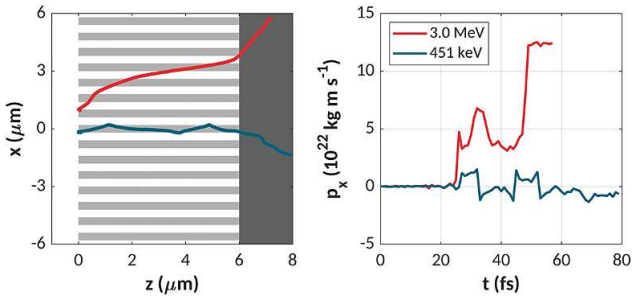

Figure 8. The transverse momenta of two example fast electrons as they traverse the wire region. The blue trajectory is for an electron with a final energy close to the ponderomotive temperature, and the red trajectory is for one of the highest energy MeV electrons.

Figure 8 evidences the effect of the guiding fields around the wires on high- and low-energy electrons as they propagate across the wire array. For a lower energy electron with $E_{max} = 400$ keV, the fields are sufficiently strong to reduce the transverse momenta to the opposite sign and effectively restrict the electron trajectory around the wire and guide it. A higher energy electron with $E_{max} = 3$ MeV experiences a similar modulation in the transverse momenta. However, the initial p_x is great enough that the change in momenta does not affect the overall trajectory significantly. The electron continues to propagate in the $+x$-direction across the wire array and does not exhibit a clear guiding along a wire structure.

Whilst evidence has been presented here demonstrating the ability of the NWs to guide the electrons under particular conditions, the geometry is clearly not optimized to reduce the final emittance. Many electrons undergo an oscillatory motion around the wires and their transverse momenta are hardly reduced by the NW structures, and are even enhanced compared to planar targets, as shown in Figures 4(e) and 4(f). Since the fields responsible for inducing the oscillatory nature of the fast electron transport are a consequence of extracting and accelerating the electrons from the wires, it may be difficult to avoid this entirely.

The larger azimuthal magnetic field at the wire–substrate boundary has been explored and identified elsewhere in intense laser interactions with planar targets[50–53], primarily on the effect on sheath-accelerated protons at the rear surface. These self-generated magnetic fields at the front surface of the target can be attributed to the 'fountain effect'[54–56] arising from the interplay between the counter-propagating injected fast electron and return currents. Fast electrons propagating through the $+B_y$ region (blue) will be deflected upwards in the x direction, and those propagating through the $-B_y$ region (red) will be deflected downwards in the $-x$ direction. This is in agreement with the observed electron trajectory deflections in Figures 5(b) and 5(c).

A consideration of these generated fields is vital for full exploitation of the wires as fast electron guiding elements. A mitigation of the defocusing magnetic field growth at the wire–substrate interface could be realized through proper choice of laser-target parameters. For example, since the strength of the magnetic field generated scales with the injected fast electron current density[57], a larger focal spot could be implemented to reduce the deflection experienced by the fast electrons accelerated in the wires. In addition, lower energy electrons appear to be more readily guided along the wires and suffer less deflection due to the **B**-field at the substrate.

Finally, we note that the 2D simulations of NW targets are inherently inaccurate to reproduce the target geometry since they model infinite 'slabs' in the y-direction. Simulation studies by Fedeli *et al.*[48] and Jiang *et al.*[31] compared the effectiveness of 2D simulations as a means of reproducing three-dimensional (3D) simulations. Whilst the qualitative results could be reproduced, there were differences observed in the final laser absorption and electron temperatures. However, the EM fields between the wire gaps should be reliably reproduced in two dimensions for this wire diameter and spacing, as should the transverse guiding of the electrons. In addition, the generation of the azimuthal **B**-field at the substrate can still be captured in two dimensions.

6. Conclusion

NW targets are frequently endorsed as a means to attain higher laser absorption into fast electrons. Enhanced coupling into fast electrons, resulting in an increased electron flux or temperature, is well-recognized, as is the potential for the wires to guide the electrons. Less attention has been paid to the transport of the electrons as they exit the influence of the wires and the effect of the wires on the overall electron beam properties. The experimental measurements reported here suggest an increased emittance of the escaping fast electron beam from the NW targets. PIC simulations explain this increase in emittance not only by an increased hot electron temperature, but also through the discovery of a self-generated magnetic field growing at the wire–substrate boundary that serves to defocus the electron beam. Further work on the use of NW targets as an efficient fast electron beam source should consider this field generation carefully. The detrimental effects on the beam emittance could be reduced by employing appropriate wire geometries and laser parameters.

Acknowledgements

We acknowledge financial support from the NextGenerationEU (PNRR) Integrated Infrastructure Initiative in Photonic and Quantum Sciences (IPHOQS) (CUP B53C22001750006, ID D2B8D520, IR0000016) and EuPRAXIA Advanced Photon Sources (EuAPS) (CUP

https://doi.org/10.1017/hpl.2025.5 Published online by Cambridge University Press

I93C21000160006, IR0000030). We also acknowledge support and funding from the Engineering and Physical Sciences Research Council (EP/L01663X/1) and the Royal Society International Exchange (IES/R3/170248). Computing resources were provided by STFC Scientific Computing Department's SCARF cluster. This work was in part funded by the UK EPSRC (grants EP/G054950/1, EP/G056803/1, EP/G055165/1 and EP/ M022463/1).

References

1. C. M. Brenner, S. R. Mirfayzi, D. R. Rusby, C. Armstrong, A. Alejo, L. A. Wilson, R. Clarke, H. Ahmed, N. M. H. Butler, D. Haddock, A. Higginson, A. McClymont, C. Murphy, M. Notley, P. Oliver, R. Allott, C. Hernandez-Gomez, S. Kar, P. McKenna, and D. Neely, Plasma Phys. Control. Fusion **58**, 014039 (2016).
2. L. A. Gizzi, A. Giulietti, D. Giulietti, P. Köster, L. Labate, T. Levato, F. Zamponi, A. Lübcke, T. Kämpfer, I. Uschmann, E. Förster, A. Antonicci, and D. Batani, Plasma Phys. Control. Fusion **49**, B211 (2007).
3. P. Köster, K. Akli, D. Batani, S. Baton, R. G. Evans, A. Giulietti, D. Giulietti, L. A. Gizzi, J. S. Green, M. Koenig, L. Labate, A. Morace, P. Norreys, F. Perez, J. Waugh, N. Woolsey, and K. L. Lancaster, Plasma Phys. Control. Fusion **51**, 014007 (2009).
4. D. R. Rusby, C. D. Armstrong, G. G. Scott, M. King, P. McKenna, and D. Neely, High Power Laser Sci. Eng. **7**, e45 (2019).
5. R. A. Snavely, M. H. Key, S. P. Hatchett, T. E. Cowan, M. Roth, T. W. Phillips, M. A. Stoyer, E. A. Henry, T. C. Sangster, M. S. Singh, S. C. Wilks, A. Mackinnon, A. Offenberger, D. M. Pennington, K. Yasuike, A. B. Langdon, B. F. Lasinski, J. Johnson, M. D. Perry, and E. M. Campbell, Phys. Rev. Lett. **85**, 2945 (2000).
6. S. C. Wilks, A. B. Langdon, T. E. Cowan, M. Roth, M. Singh, S. Hatchett, M. H. Key, D. Pennington, A. MacKinnon, and R. A. Snavely, Phys. Plasmas **8**, 542 (2001).
7. Y. Sentoku, T. E. Cowan, A. Kemp, and H. Ruhl, Phys. Plasmas **10**, 2009 (2003).
8. V. Malka, S. Fritzler, E. Lefebvre, E. d'Humières, R. Ferrand, G. Grillon, C. Albaret, S. Meyroneinc, J.-P. Chambaret, A. Antonetti, and D. Hulin, Med. Phys. **31**, 1587 (2004).
9. S. Malko, W. Cayzac, V. Ospina-Bohórquez, K. Bhutwala, M. Bailly-Grandvaux, C. McGuffey, R. Fedosejevs, X. Vaisseau, A. Tauschwitz, J. I. Apiñaniz, D. De Luis Blanco, G. Gatti, M. Huault, J. A. Perez Hernandez, S. X. Hu, A. J. White, L. A. Collins, K. Nichols, P. Neumayer, G. Faussurier, J. Vorberger, G. Prestopino, C. Verona, J. J. Santos, D. Batani, F. N. Beg, L. Roso and L. Volpe, Nat. Commun. **13**, 2893 (2022).
10. M. Tabak, J. Hammer, M. E. Glinsky, W. L. Kruer, S. C. Wilks, J. Woodworth, E. M. Campbell, M. D. Perry, and R. J. Mason, Phys. Plasmas **1**, 1626 (1994).
11. O. Culfa, G. J. Tallents, A. K. Rossall, E. Wagenaars, C. P. Ridgers, C. D. Murphy, R. J. Dance, R. J. Gray, P. McKenna, C. D. R. Brown, S. F. James, D. J. Hoarty, N. Booth, A. P. L. Robinson, K. L. Lancaster, S. A. Pikuz, A. Y. Faenov, T. Kampfer, K. S. Schulze, I. Uschmann, and N. C. Woolsey, Phys. Rev. E **93**, 043201 (2016).
12. J. J. Honrubia and J. Meyer-ter-Vehn, Nucl. Fusion **46**, L25 (2006).
13. J. S. Green, V. M. Ovchinnikov, R. G. Evans, K. U. Akli, H. Azechi, F. N. Beg, C. Bellei, R. R. Freeman, H. Habara, R. Heathcote, M. H. Key, J. A. King, K. L. Lancaster, N. C. Lopes, T. Ma, A. J. MacKinnon, K. Markey, A. McPhee, Z. Najmudin, P. Nilson, R. Onofrei, R. Stephens, K. Takeda, K. A. Tanaka, W. Theobald, T. Tanimoto, J. Waugh, L. Van Woerkom, N. C. Woolsey, M. Zepf, J. R. Davies, and P. A. Norreys, Phys. Rev. Lett. **100**, 015003 (2008).
14. A. Debayle, J. J. Honrubia, E. d'Humières, and V. T. Tikhonchuk, Phys. Rev. E **82**, 036405 (2010).
15. C. Bellei, L. Divol, A. J. Kemp, M. H. Key, D. J. Larson, D. J. Strozzi, M. M. Marinak, M. Tabak, and P. K. Patel, Phys. Plasmas **20**, 052704 (2013).
16. C. D. Armstrong, G. Liao, H. Liu, Y. Li, Z. Zhang, Y. Zhang, B. Zhu, P. Bradford, N. C. Woolsey, P. Oliveira, C. Spindloe, W. Wang, P. McKenna, and D. Neely, Plasma Phys. Control. Fusion **61**, 034001 (2019).
17. P. Mora, Phys. Rev. Lett. **90**, 185002 (2003).
18. Y. Takagi, N. Iwata, E. D'Humieres, and Y. Sentoku, Phys. Rev. Res. **3**, 043140 (2021).
19. C. M. S. Sears, A. Buck, K. Schmid, J. Mikhailova, F. Krausz, and L. Veisz, Phys. Rev. Spec. Top. Accel. Beams **13**, 092803 (2010).
20. A. Cianchi, D. Alesini, M. P. Anania, A. Bacci, M. Bellaveglia, M. Castellano, E. Chiadroni, D. Di Giovenale, G. P. Di Pirro, M. Ferrario, A. Gallo, L. Innocenti, A. Mostacci, R. Pompili, A. R. Rossi, J. Scifo, V. Shpakov, C. Vaccarezza, and F. Villa, Phys. Rev. Spec. Topic. Accel. Beams **18**, 082804 (2015).
21. V. Shpakov, M. P. Anania, M. Behtouei, M. Bellaveglia, A. Biagioni, M. Cesarini, E. Chiadroni, A. Cianchi, G. Costa, M. Croia, A. Del Dotto, M. Diomede, F. Dipace, M. Ferrario, M. Galletti, A. Giribono, A. Liedl, V. Lollo, L. Magnisi, A. Mostacci, G. Di Pirro, L. Piersanti, R. Pompili, S. Romeo, A. R. Rossi, J. Scifo, C. Vaccarezza, F. Villa, and A. Zigler, Phys. Rev. Accel. Beams **24**, 051301 (2021).
22. S. Mondal, I. Chakraborty, S. Ahmad, D. Carvalho, P. Singh, A. D. Lad, V. Narayanan, P. Ayyub, G. R. Kumar, J. Zheng, and Z. M. Sheng, Phys. Rev. B **83**, 035408 (2011).
23. G. Cristoforetti, P. Londrillo, P. K. Singh, F. Baffigi, G. D'Arrigo, A. D. Lad, R. G. Milazzo, A. Adak, M. Shaikh, D. Sarkar, G. Chatterjee, J. Jha, M. Krishnamurthy, G. R. Kumar, and L. A. Gizzi, Sci. Rep. **7**, 1479 (2017).
24. R. Xie, L. H. Cao, Y. Chao, Y. Jiang, Z. J. Liu, C. Y. Zheng, and X. T. He, Phys. Plasmas **27**, 123108 (2020).
25. E. Eftekhari-Zadeh, M. S. Blümcke, Z. Samsonova, R. Loetzsch, I. Uschmann, M. Zapf, C. Ronning, O. N. Rosmej, D. Kartashov, and C. Spielmann, Phys. Plasmas **29**, 013301 (2022).
26. J. J. Rocca, M. G. Capeluto, R. C. Hollinger, S. Wang, Y. Wang, G. R. Kumar, A. D. Lad, A. Pukhov, and V. N. Shlyaptsev, Optica **11**, 437 (2024).
27. P. K. Singh, G. Chatterjee, A. D. Lad, A. Adak, S. Ahmed, M. Khorasaninejad, M. M. Adachi, K. S. Karim, S. S. Saini, A. K. Sood, and G. R. Kumar, Appl. Phys. Lett. **100**, 244104 (2012).
28. S. Jiang, L. L. Ji, H. Audesirk, K. M. George, J. Snyder, A. Krygier, P. Poole, C. Willis, R. Daskalova, E. Chowdhury, N. S. Lewis, D. W. Schumacher, A. Pukhov, R. R. Freeman, and K. U. Akli, Phys. Rev. Lett. **116**, 085002 (2016).
29. D. Khaghani, M. Lobet, B. Borm, L. Burr, F. Gärtner, L. Gremillet, L. Movsesyan, O. Rosmej, M. E. Toimil-Molares, F. Wagner, and P. Neumayer, Sci. Rep. **7**, 11366 (2017).
30. A. Moreau, R. Hollinger, C. Calvi, S. Wang, Y. Wang, M. G. Capeluto, A. Rockwood, A. Curtis, S. Kasdorf, V. N. Shlyaptsev, V. Kaymak, A. Pukhov, and J. J. Rocca, Plasma Phys. Control. Fusion **62**, 014013 (2020).
31. S. Jiang, A. G. Krygier, D. W. Schumacher, K. U. Akli, and R. R. Freeman, Phys. Rev. E **89**, 013106 (2014).
32. Z. Zhao, L. Cao, L. Cao, J. Wang, W. Huang, W. Jiang, Y. He, Y. Wu, B. Zhu, K. Dong, Y. Ding, B. Zhang, Y. Gu, M. Y. Yu, and X. T. He, Phys. Plasmas **17**, 123108 (2010).

https://doi.org/10.1017/hpl.2025.5 Published online by Cambridge University Press

33. Y. Yamazaki, T. Kurihara, H. Kobayashi, I. Sato, and A. Asami, Nucl. Instrum. Methods Phys. Res., Sect. A **322**, 139 (1992).
34. M. Zhang, "Emittance formula for slits and pepper-pot measurement", FERMILAB-TM-1998 (1996).
35. L. A. Gizzi, L. Labate, F. Baffigi, F. Brandi, G. Bussolino, L. Fulgentini, P. Köster, and D. Palla, High Power Laser Sci. Eng. **9**, e10 (2021).
36. D. Calestani, M. Villani, G. Cristoforetti, F. Brandi, P. Köster, L. Labate, and L. A. Gizzi, Matter Radiat. Extremes **6**, 046903 (2021).
37. G. Cristoforetti, A. Anzalone, F. Baffigi, G. Bussolino, G. D'Arrigo, L. Fulgentini, A. Giulietti, P. Köster, L. Labate, S. Tudisco, and L. A. Gizzi, Plasma Phys. Control. Fusion **56**, 095001 (2014).
38. T. D. Arber, K. Bennett, C. S. Brady, A. Lawrence-Douglas, M. G. Ramsay, N. J. Sircombe, P. Gillies, R. G. Evans, H. Schmitz, A. R. Bell, and C. P. Ridgers, Plasma Phys. Control. Fusion **57**, 113001 (2015).
39. S. C. Wilks, W. L. Kruer, M. Tabak, and A. B. Langdon, Phys. Rev. Lett. **69**, 1383 (1992).
40. M. Sherlock, Phys. Plasmas **16**, 103101 (2009).
41. A. Macchi, Phys. Plasmas **25**, 031906 (2018).
42. G. Cristoforetti, F. Baffigi, F. Brandi, G. D'Arrigo, A. Fazzi, L. Fulgentini, D. Giove, P. Köster, L. Labate, G. Maero, D. Palla, M. Romé, R. Russo, D. Terzani, P. Tomassini, and L. A. Gizzi, Plasma Phys. Control. Fusion **62**, 114001 (2020).
43. L. A. Gizzi, G. Cristoforetti, F. Baffigi, F. Brandi, G. D'Arrigo, A. Fazzi, L. Fulgentini, D. Giove, P. Köster, L. Labate, G. Maero, D. Palla, M. Romé, M. Russo, D. Terzani, and P. Tomassini, Phys. Rev. Res. **2**, 033451 (2020).
44. G. Chatterjee, P. K. Singh, S. Ahmed, A. P. L. Robinson, A. D. Lad, S. Mondal, V. Narayanan, I. Srivastava, N. Koratkar, J. Pasley, A. K. Sood, and G. R. Kumar, Phys. Rev. Lett. **108**, 235005 (2012).
45. D. B. Zou, D. Y. Yu, X. R. Jiang, M. Y. Yu, Z. Y. Chen, H. B. Zhuo, C. T. Zhou, and S. C. Ruan, Phys. Plasmas **26**, 123105 (2019).
46. Y. Ji, G. Jiang, W. Wu, C. Wang, Y. Gu, and Y. Tang, Appl. Phys. Lett. **96**, 041504 (2010).
47. Y. Tian, J. Liu, W. Wang, C. Wang, X. Lu, Y. Leng, X. Liang, R. Li and Z. Xu, Plasma Phys. Control. Fusion **56**, 075021 (2014).
48. L. Fedeli, A. Formenti, L. Cialfi, A. Pazzaglia, and M. Passoni, Sci. Rep. **8**, 3834 (2018).
49. J. Wang, Z. Q. Zhao, W. H. He, L. H. Cao, K. G. Dong, Y. C. Wu, B. Zhu, T. K. Zhang, B. Zhang, Z. M. Zhang, and Y. Q. Gu, Phys. Plasmas **21**, 103111 (2014).
50. L. A. Gizzi, A. J. Mackinnon, D. Riley, S. M. Viana, and O. Willi, Laser Particle Beams **13**, 511 (1995).
51. G. Sarri, A. Macchi, C. A. Cecchetti, S. Kar, T. V. Liseykina, X. H. Yang, M. E. Dieckmann, J. Fuchs, M. Galimberti, L. A. Gizzi, R. Jung, I. Kourakis, J. Osterholz, F. Pegoraro, A. P. L. Robinson, L. Romagnani, O. Willi, and M. Borghesi, Phys. Rev. Lett. **109**, 205002 (2012).
52. B. Albertazzi, S. N. Chen, P. Antici, J. Böker, M. Borghesi, J. Breil, V. Dervieux, J. L. Feugeas, L. Lancia, M. Nakatsutsumi, Ph. Nicolai, L. Romagnagni, R. Shepherd, Y. Sentoku, M. Starodubtsev, M. Swantusch, V. T. Tikhonchuk, O. Willi, E. d'Humières, H. Pépin, and J. Fuchs, Phys. Plasmas **22**, 123108 (2015).
53. M. Nakatsutsumi, Y. Sentoku, A. Korzhimanov, S. N. Chen, S. Buffechoux, A. Kon, B. Atherton, P. Audebert, M. Geissel, L. Hurd, M. Kimmel, P. Rambo, M. Schollmeier, J. Schwarz, M. Starodubtsev, L. Gremillet, R. Kodama, and J. Fuchs, Nat. Commun. **9**, 280 (2018).
54. Y. Sakagami, H. Kawakami, S. Nagao, and C. Yamanaka, Phys. Rev. Lett. **42**, 839 (1979).
55. P. Kolodner and E. Yablonovitch, Phys. Rev. Lett. **43**, 1402 (1979).
56. A. Pukhov, Phys. Rev. Lett. **86**, 3562 (2001).
57. W. Schumaker, N. Nakanii, C. McGuffey, C. Zulick, V. Chyvkov, F. Dollar, H. Habara, G. Kalintchenko, A. Maksimchuk, K. A. Tanaka, A. G. R. Thomas, V. Yanovsky, and K. Krushelnick, Phys. Rev. Lett. **110**, 015003 (2013).

https://doi.org/10.1017/hpl.2025.5 Published online by Cambridge University Press